Available online at www.sciencedirect.com
ScienceDirect
International Journal of Heat and Fluid Flow 27 (2006) 994–1009
International Journal of HEAT AND FLUID FLOW
www.elsevier.com/locate/ijhff

Turbulent flow around a wall-mounted cube: A direct numerical simulation

Alexander Yakhot [a,*], Heping Liu [a,1], Nikolay Nikitin [b]

[a] The Pearlstone Center for Aeronautical Engineering Studies, Department of Mechanical Engineering, Ben-Gurion University of the Negev, Beersheva Beersheva 84105, Israel
[b] Institute of Mechanics, Moscow State University, 1 Michurinski Prospekt, 119899 Moscow, Russia

Received 24 August 2004; received in revised form 29 December 2005; accepted 3 February 2006
Available online 12 May 2006

Abstract

An immersed-boundary method was employed to perform a direct numerical simulation (DNS) of flow around a wall-mounted cube in a fully developed turbulent channel for a Reynolds number $Re = 5610$, based on the bulk velocity and the channel height. Instantaneous results of the DNS of a plain channel flow were used as a fully developed inflow condition for the main channel. The results confirm the unsteadiness of the considered flow caused by the unstable interaction of a horseshoe vortex formed in front of the cube and on both its sides with an arch-type vortex behind the cube. The time-averaged data of the turbulence mean-square intensities, Reynolds shear stresses, kinetic energy and dissipation rate are presented. The negative turbulence production is predicted in the region in front of the cube where the main horseshoe vortex originates.

Keywords: Turbulence; Direct numerical simulation; Negative turbulence production; Immersed-boundary method

1. Introduction

Flow and heat transfer in a channel with wall-mounted cubes represent a general engineering configuration that is relevant in many applications. Owing to simple geometry but with complex vortical structures and generic flow phenomena associated with a turbulent flow, this configuration has attracted increasing attention from researchers and has been used for the bench-marking purposes to validate turbulent models and numerical methods.

Before the 1990s, measurements of three-dimensional flows around wall-mounted cubical obstacles were unavailable. Instead any understanding of the major global features of flow patterns were based on flow visualization studies. The first published measurements of the turbulent velocity field, energy balance and heat transfer around a surface-mounted cube begun to appear in the 1990s. Several experimental works have been performed on a flow around a single wall-mounted cube in a developed turbulent channel flow. Results showed that this flow is characterized by the appearance of a horseshoe-type vortex at the windward face, an arc-shaped vortex in the wake of the cube, flow separation at the top and side face of the cube and vortex shedding. The flow features and experimental data for time-averaged flow quantities have been well documented in Martinuzzi and Tropea (1993) and Hussein and Martinuzzi (1996). Nakamura et al. (2001) experimentally investigated a fluid flow and local heat transfer around a cube mounted on a wall of a plane channel. The turbulent boundary layer thickness was about two times higher than the cube height. Meinders et al. (1999) experimental study was also performed in a developing turbulent channel flow.

The ability to perform these measurement aroused great interest in numerical simulation of these flows. Most numerical studies were performed by using the Reynolds-

* Corresponding author.
E-mail address: yakhot@bgu.ac.il (A. Yakhot).
[1] Present address: Central Iron and Steel Research Institute, 76 Xueyuan NanLu, Beijing 100081, People's Republic of China.

0142-727X/$ - see front matter © 2006 Elsevier Inc. All rights reserved.
doi:10.1016/j.ijheatfluidflow.2006.02.026

Nomenclature

Δ	mean grid spacing, $(\Delta_x\Delta_y\Delta_z)^{1/3}$
δ	boundary layer thickness
$\overline{\varepsilon}$	dissipation rate of the turbulence energy
η_K	Kolmogorov's length scale, $(\nu^3/\overline{\varepsilon})^{1/4}$
K	turbulence kinetic energy, $0.5(\overline{u'^2}+\overline{v'^2}+\overline{w'^2})$
ν	kinematic viscosity
$\overline{u_i'u_j'}$	Reynolds stresses, $i, j = x, y, z$
ρ	density
τ_w	wall shear stress
$\mathbf{u}$	velocity vector
$\overline{u'^2}, \overline{v'^2}, \overline{w'^2}$	turbulence mean-square intensities
f	frequency
H	height of the channel
h	height of the cube
p	kinematic (divided by density) pressure
P_K	production rate of turbulence kinetic energy, $\overline{u_i'u_j'}S_{ij}$
Re_h	Reynolds number, $U_m h/\nu$
Re_m	Reynolds number, $U_m H/\nu$
S_{ij}	rate of strain tensor, $0.5(\partial U_i/\partial x_j + \partial U_j/\partial x_i)$, $i, j = x, y, z$
St	Strouhal number, fh/U_m
u', v', w'	fluctuating velocity components in x-, y- and z-directions
U, V, W	mean velocity components in x-, y- and z-directions
U_m	mean velocity
u_τ	friction velocity, $\sqrt{\tau_w/\rho}$
x, y, z	steamwise, wall-normal and spanwise directions

averaged Navier–Stokes (RANS) method with different turbulent models (Iaccarino et al., 2003; Lakehal and Rodi, 1997) and large-eddy simulations (LES) (Krajnović and Davidson, 1999, 2001; Niĉeno et al., 2002; Rodi et al., 1997; Shah and Ferziger, 1997). For the flow considered in the present study, RANS approach could not reproduce the details of the complex fluid structure near the wall, e.g. the converging–diverging horseshoe vortex and separation of the boundary layer in front of the cube, nor the separation length behind the cube. It is commonly believed that this inability is due to the disregard of unsteady effects such as vortex shedding. In contrast, global flow features and characteristics predicted by LES and more recently by unsteady RANS-based modeling (Iaccarino et al., 2003) showed good agreement with experimental data.

A numerical study of the fundamental hydrodynamic effects in complex geometries is a challenging task for discretization of Navier–Stokes equations in the vicinity of complex geometry boundaries. Implementing boundary-fitted, structured or unstructured grids in finite element methods help to deal with this problem, however the numerical algorithms designed for such grids are usually inefficient in comparison to those designed for simple rectangular meshes. This disadvantage is particularly pronounced for simulating non-steady incompressible flows when the Poisson equation for the pressure has to be solved at each time step. Iterative methods for complex meshes have low convergence rates, especially for fine grids. On the other hand, very efficient and stable algorithms have been developed for solving Navier–Stokes equations in rectangular domains. In particular, these algorithms use fast direct methods for solving the Poisson's equation for the pressure (Swarztrauber, 1974). The evident simplicity and other advantages of such solvers led to the development of approaches for formulating complex geometry flows on simple rectangular domains.

One such approach is based on the immersed-boundary (IB) method originally introduced to reduce the simulation of complex geometry flows to that defined on simple (rectangular) domains. This can be illustrated if we consider a flow of an incompressible fluid around an obstacle Ω (S is its boundary) placed into a rectangular domain (Π). To impose the no-slip condition on an obstacle surface S (which becomes an internal surface for the rectangular domain wherein the problem is formulated), a source term $\mathbf{f}$ (an artificial body force) is added to the Navier–Stokes equations. The purpose of the forcing term is to impose the no-slip boundary condition on the $\mathbf{x}_S$-points which define the immersed boundary S.

Immersed-boundary-based methods are considered to be a powerful tool for simulating complex flows. Different immersed-boundary methods can be found in Balaras (2004), Fadlun et al. (2000), Kim et al. (2001), Tseng and Ferziger (2003). IB-based approaches differ by the method used to introduce an artificial force into the governing equations. Fadlun et al. (2000) and Kim et al. (2001) developed the idea of "direct forcing" for implementing finite-volume methods on a staggered grid. Kim et al. (2001) contributed two basic approaches for introducing direct forcing when using immersed-boundary methods. One was a numerically stable interpolation procedure for evaluating the forcing term, and the other introducing a mass source/sink to enhance the solution's accuracy.

The main advantages of IB methods are that they are based on relatively simple numerical codes and highly effective algorithms, resulting in considerable reduction of required computing resources. The main disadvantage, however, is the difficulty in resolving local regions with extreme variations of flow characteristics. These are especially pronounced for high Reynolds number flows. Moreover, in order to impose the boundary conditions, numerical algorithms require that the node velocity values be interpolated onto the boundary points because the boundary S does not coincide with the gridpoints of a rectangular mesh. Finally, due to the time-stepping algorithms

used, for example, in "direct forcing" IB methods, the no-slip boundary condition is imposed with $O(\Delta t^2)$ accuracy. Therefore, implementation of IB methods to simulate turbulent flows requires careful monitoring to avoid possible contamination of numerical results arising from inaccurate boundary conditions.

All of the aforementioned numerical studies used indirect methods to test the various modeling approaches. However, it is often difficult to judge the adequacy of a turbulence model due to uncertainties of the verifiability of available experimental data. Due to the vast, continuous range of excited scales of motion, which must be correctly resolved by numerical simulation, the DNS approach is the most accurate but, unfortunately, it is also the most expensive. Any DNS simulation, especially in complex geometry, is very time consuming and has extensive storage requirements. At present, the application of the DNS to realistic flows of engineering importance is restricted by relatively low Reynolds numbers. The objective of DNS not necessarily for reproducing real-life flows, but performing a controlled study that allows better insight into flow physics in order to develop turbulence modeling approaches. This is the first paper to present DNS-based simulations carried out with inlet boundary conditions which are physically realistic and without the use of turbulence models. Our major concern was to perform the DNS of a case that yields reliable results. The aims of this work were to test the recent trend to employ immersed-boundary methods for simulating turbulent flows and to examine the feasibility of using DNS for complex geometry flows. We present the time-averaged data of the following turbulence statistics: mean-square intensities, Reynolds shear stress, kinetic energy and dissipation rate. We draw attention to the occurrence of negative turbulence kinetic energy production in front of the cube that is relevant for turbulence LES/RANS modeling.

2. Numerical method

The flow of an incompressible fluid around an obstacle Ω placed into a rectangular domain (Π) is governed by the Navier–Stokes and incompressibility equations with the no-slip boundary condition. The basic idea of IB methods is to describe a problem, defined in $\Pi - \Omega$, by solving the governing equations inside an entire rectangular Π *without* an obstacle, which allows using simple rectangular meshes. To impose boundary conditions on an obstacle surface S (which becomes an internal surface for the rectangular domain where the problem is formulated), we add a body force $\mathbf{f}$ term to the governing equations:

$$\frac{\partial \mathbf{u}}{\partial t} = -(\mathbf{u}\nabla)\mathbf{u} - \nabla p + \nu\nabla^2\mathbf{u} + \mathbf{f} \tag{1}$$

where $\mathbf{u}$ is the velocity, p is the kinematic (divided by density) pressure and ν is the kinematic viscosity.

The numerical solution to the system of equation (1) was obtained by using the IB approach suggested by Kim et al. (2001). The only difference is that instead of the time-advancing scheme used in Kim et al. (2001), we employed another third-order Runge–Kutta algorithm suggested in Nikitin (1996). This time-treatment results in a calculation procedure allowing numerical accuracy and time-step control.

3. Numerical simulation: problem formulation

3.1. Computational domain, spatial and temporal resolution

A configuration of a channel with a wall-mounted cube is shown in Fig. 1. The computational domain is $14h \times 3h \times 6.4h$ in the streamwise (x), normal to the channel walls (y) and spanwise (z) directions, respectively, where h is the cube's height. The computational domain inlet and outlet are located at $x = -3h$ and $x = 11h$, respectively, and the cube is located between $0 \leqslant x \leqslant h$, $0 \leqslant y \leqslant h$, $-0.5h \leqslant z \leqslant 0.5h$. A computational grid is set of $181 \times 121 \times 256$ gridpoints in the x, y and z directions, respectively. A non-uniform mesh was used in the streamwise and wall-normal directions with gridpoints clustering near the channel and cube walls. The finest grid spacing is of order $\Delta x_{\min} = 0.024h$ near the cube's front and rear walls and $\Delta y_{\min} = 0.006h$ near the channel and cube's top walls.

The computational domain also contains an *entrance* channel, which is not shown in Fig. 1. To generate a fully developed turbulent flow to be used as the inlet condition to the channel with a cube, DNS was performed in an entrance channel measuring $9h \times 3h \times 6.4h$. A computational grid in the entrance channel measured $64 \times 121 \times 256$ gridpoints in the x, y and z directions, respectively. The total number of 7,589,120 gridpoints were used. For the grid refinement tests,[2] the number of gridpoints was 11,009,280. The computations have been performed on CRAY SV1 Supercomputer, maximum memory used −115 MW, CPU-time is 70 s/time step.

A uniform mesh of $\Delta x = 0.141h$ was used in the streamwise direction. In the wall-normal direction, the gridpoints were clustered near the channel walls with $\Delta y_{\min} = 0.006h$. For both the entrance and main channels, in the spanwise z-direction, the gridpoints were equally spaced with $\Delta z = 0.025h$. The computational grid data are summarized in Table 1. The subscript "+" denotes that a quantity is normalized by the wall units: the characteristic length, $l_\tau = \nu/u_\tau$, and velocity, $u_\tau = (\tau_w/\rho)^{1/2}$, computed for the fully developed flow in the entrance channel. For isotropic and homogenous turbulence, the Kolmogorov's length scale, $\eta_K = (\nu^3/\overline{\mathscr{E}})^{1/4}$ ($\overline{\mathscr{E}} = \nu\overline{\frac{\partial u_i'}{\partial x_j}\frac{\partial u_i'}{\partial x_j}}$ is the mean dissipation rate of the turbulence energy) is the *smallest* scale to be spatially resolved. The flow considered in this paper exhibits strong anisotropy. However, an estimation of the smallest

[2] Gridpoints were added near the front and top cube's faces and near the channel base.

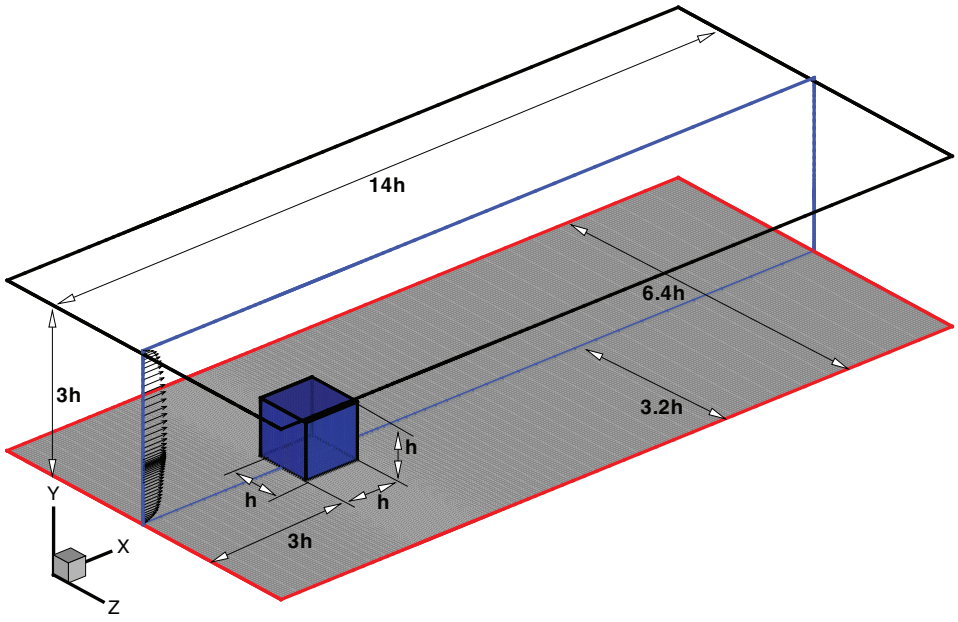

Fig. 1. Geometry of a cube mounted on a wall.

Table 1
Computational domain and grid data

Domain	Main channel	Entrance channel
$L_x \times L_y \times L_z$	$14h \times 3h \times 6.4h$	$9h \times 3h \times 6.4h$
$N_x \times N_y \times N_z$	$181 \times 121 \times 256$	$64 \times 121 \times 256$
Cube grid	$40 \times 51 \times 40$	
Δx^+	3.1–40.7	19.51
Δy^+	0.76–6.46	0.76–6.46
Δz^+	3.46	3.46

scale, l_d, to be spatially resolved by numerical simulating the anisotropic turbulence is beyond the scope of this paper. It is believed that the mean grid width $\Delta = (\Delta_x\Delta_y\Delta_z)^{1/3}$ is $O(\eta_K)$ and is typically greater than η_K. DNS-based results reported in the literature show good agreement with experimental data even though the Kolmogorov's length scale was not resolved, e.g. $\Delta/\eta_K = \gamma > 1$ (Moin and Mahesh, 1998). Moser and Moin (1987) note that in a curved channel, most of the dissipation occurs at scales greater than $15\eta_K$. For simulations of the wall-bounded turbulence in simple geometries (channel, pipe, boundary layer), η_K reaches the smallest values in the near-wall regions where the dissipation rate, $\overline{\varepsilon}$, is expected to be maximal. For complex geometry simulations, η_K is unknown a priori. As an a posteriori test, we computed Kolmogorov's length scale. Table 2 summarizes the data of the spatial resolution in the near-cube region. In our simulations, we found that $2.0 < \gamma, \gamma_x, \gamma_y, \gamma_z < 5.0$ in the regions of complex vortical flows of the horseshoe, lateral and top vortices. The relatively high (>5) values of γ_y and γ_z were detected in the vicinity of the sharp edges of the cube. The high values of $\gamma_x > 6$ were found in the recovery region, downstream to the rear vortex reattachment point. Note that ad hoc computing the smallest scales that need to be resolved as $l_d \equiv \eta_K$ leads to an *underestimating* of l_d. This is because computing the dissipation rate from $\overline{\varepsilon} = \nu\overline{\frac{\partial u_i'}{\partial x_j}\frac{\partial u_i'}{\partial x_j}}$ results in *overestimating* $\overline{\varepsilon}$ since all the scales are accounted for, including those which are strongly anisotropic and do not in fact lead to energy dissipation.

Cartesian coordinates with a staggered grid was employed for spatial finite-difference discretization. The second-order central difference scheme was used for the convection and viscous terms of the Navier–Stokes equations. The imposing no-slip boundary conditions and incompressibility were combined into a single time-step procedure. A periodic boundary condition was imposed in the spanwise direction, the no-slip boundary condition was used at all rigid walls and the Neumann condition was used for pressure at all

Table 2
Comparison of computational resolution around the cube with Kolmogorov's length scale, $1.5 < x/h < 6.0$, $0 < y/h < 2.0$, $-1.0 < z/h < 1.0$, $\Delta = \gamma\eta_K$, $\Delta = (\Delta_x\Delta_y\Delta_z)^{1/3}$, $\eta_K = (\nu^3/\overline{\varepsilon})^{1/4}$

$\gamma = \Delta/\eta_K$	γ-range	Cells with $3 < \gamma < 4$ (%)	Cells with $4 < \gamma < 5$ (%)	Cells with $5 < \gamma < 6$ (%)	Cells with $\gamma > 6$ (%)
γ_x	0.5–14.0	16.3	9.5	3.8	9.1
γ_y	0.2–7.2	7.3	2.7	0.6	0.04
γ_z	0.5–9.6	16.0	4.2	0.4	0.07
γ	0.4–5.9	13.7	4.2	5.2	–

boundaries. At the downstream outlet boundary, convective velocity conditions were imposed.

3.2. Inflow condition: fully developed turbulent channel flow

Numerical simulation of spatially developing turbulent flows requires specification of time-dependent inflow conditions. In cases with flow separation, free shear layers, laminar-turbulent transitional flows, the downstream flow is highly dependent on the conditions specified at the inlet. For studying flows around bluff bodies placed into a developing boundary layer, a possible approach is to employ a mean velocity profile and a level of turbulent kinetic energy (if those are available from the experiment). Then, a small time-dependent perturbation can be imposed on the inflow to obtain the desired statistics. Evidently, this implies that the inflow satisfies the Navier–Stokes equations, which may require excessively long streamwise domains for the developing boundary layer simulations. Imposing experimentally-obtained inflow conditions are not within the scope of this study due to their insuperable complexity. For example, in Meinders et al. (1999), the flow around a cube consisted of a developing turbulent boundary layer flow near the channel wall where the cube was placed ($\delta/h > 1$, δ is the boundary layer thickness) and an almost laminar boundary layer at the opposite wall with the core flow remaining uniform. In the present study, the oncoming flow is a fully developed turbulent channel flow. We introduce an entrance (upstream) domain which is much less costly. In this domain, the inflow is computed using periodic boundary conditions. These simulations were run simultaneously with the main computation procedure in order to specify the fully developed inflow condition. The dimensions and grid data of the entrance channel are summarized in Table 1; the first gridpoint was at $y^+ = 0.76$. The Reynolds number based on the bulk velocity and the channel height is $Re_m = 5610$, identical to the benchmark simulations of Kim et al. (1987). The calculated root-mean-square velocity fluctuations and the Reynolds shear stress profiles were compared with the results of Kim et al. (1987) showing very good agreement between the results.

4. Results and discussion

All flow parameters presented in this section are non-dimensionalized, unless they are explicitly written in the dimensional form; the cube's height, h, and the mean velocity U_m are characteristic length and velocity, respectively.

A detailed experimental investigation by Meinders et al. (1999) was performed for Reynolds numbers ranging between $2750 < Re_h < 4970$, based on the bulk velocity and the cube height. The flow visualization results were found to be independent of Re_h in the range of $2000 < Re_h < 7000$. The present computations have been performed at the relatively low Reynolds number of $Re_h = 1870$. The experiments were carried out in a two-dimensional channel with a ratio of $H/h = 3.3$, where H is the channel height. The case of $H/h = 2$ served as a test case at the Rottach–Egern large-eddy simulation (LES) workshop for two Reynolds numbers $Re_h = 3000$ and 40,000. The LES calculations showed that the flow behavior at the two Reynolds number is very similar (Rodi et al., 1997).

4.1. Flow pattern

Past experiments have been performed for both relatively low and moderate Reynolds number flows. After the first experimental study carried out by Martinuzzi and Tropea (1993) at $Re_h = 40{,}000$, a series of works were published by Meinders and co-authors (Meinders et al., 1998, 1999; Meinders and Hanjalić, 1999, 2002). Visualization and measurements indicated that the flow possesses very complex features. The flow separates in front of the cube and at its front corners on the top (roof) and side walls. The main vortex forms a horseshoe-type vortex around the cube and interacts with the main separation region behind the cube. Up to four separation regions are instantaneously disclosed.

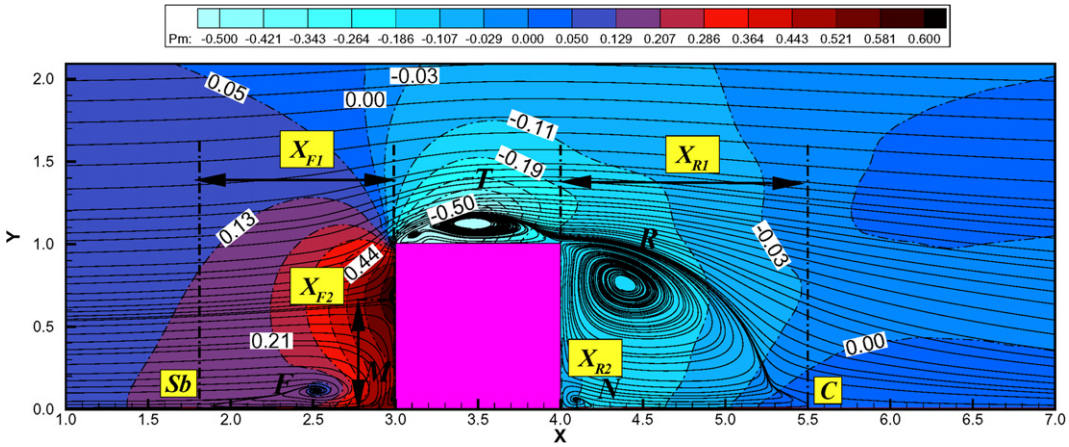

Fig. 2. Time-averaged streamlines and pressure distribution on the symmetry plane.

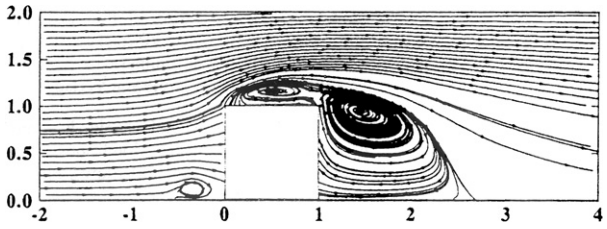

Fig. 3. Time-averaged streamlines in the symmetry plane obtained by Martinuzzi (see Rodi et al. (1997)).

Fig. 2 shows the time-averaged streamlines and pressure distribution (the background color) at the symmetry plane. The experimental outline of time-averaged streamlines obtained by Martinuzzi (see Rodi et al. (1997)) at a high Reynolds number ($Re_h = 40{,}000$) is depicted in Fig. 3. It can be seen that, despite the different Reynolds numbers, the general flow features and the overall prediction of the front, top and rear vortex modes (marked *F*, *T* and *R*) are quite similar, although some differences are visible. In our simulations for lower Reynolds numbers, there are two small counter-clockwise secondary vortices found in the bottom corner part of the front face (marked *M*) and the rear face (marked *N*); the horseshoe-type vortex, formed by the separation region in the front and bent around the cube, is initiated more upstream (marked X_{F1}) and the predicted reattachment length (marked X_{R1}) of the primary vortex behind the cube is shorter. Moreover, the flow reattaches on the cube's top surface. These predicted features differ from the high Reynolds number case of Martinuzzi and Tropea (1993), but they are in good agreement with the experimental study of Meinders et al. (1999) carried out in a developing turbulent channel flow at a low Reynolds number. In their experiment, Meinders et al. (1999) also observed flow reattachment on the top surface and the shorter wake recirculation region. In the present case, the windward separation point (marked *Sb*) is located much further downstream ($1.21h$) than in their experiment (about $1.4h$). This difference may be caused by different inflow conditions, namely, the fully developed turbulent channel flow used by us and the developing flow in Meinders et al. (1999). The predicted by us value of the front separation region $X_{F1} = 1.21h$ lies between the values of $1.0h$ and $1.4h$ measured in Martinuzzi and Tropea (1993) and Meinders et al. (1999), respectively. The front stagnation point $X_{F2} = 0.65h$, where the flow is spread radially, and the rear stagnation point $X_{R2} = 0.15h$, where an upward flow is formed, can also be seen from Fig. 2. These values agree with those found by Nakamura et al. (2001) for a wall-mounted cube in a turbulent boundary layer.

Fig. 4 depicts the near-wall ($y/h = 0.003$) and near-top-surface ($\Delta y/h = 0.003$) distribution of the time-averaged streamlines and pressure. All marked points in this figure correspond to those used in the oil-film visualization in Meinders et al. (1999) (not shown here). All flow features detected in Meinders et al. (1999) can be seen also from our results. The oncoming flow separates at the saddle point (marked *Sb*) located approximately 1.21 cube height in the front of the cube, where streamlines extend downstream along the channel floor past the sides of the cube. Just ahead of the cube, the flow separation line (marked *Sa*) is deflected downstream along the leading side faces to form two legs of a horseshoe vortex (marked *A*). The converging–diverging streamlines inside the horseshoe vortex show traces of this vortex and delineate its extent of separation. Fig. 4 shows that the flow separations from the cube's side and top faces form a complex vortical structure consisting of two side vortices (marked *E*) and the top vortex (marked by *T* in Fig. 2). Behind the cube, the flow reattachment from the side flow and the shear layer formed over the cube lead to an arc-shaped vortex tube. A pair of counter-rotating flows (marked *B*) close to the base wall

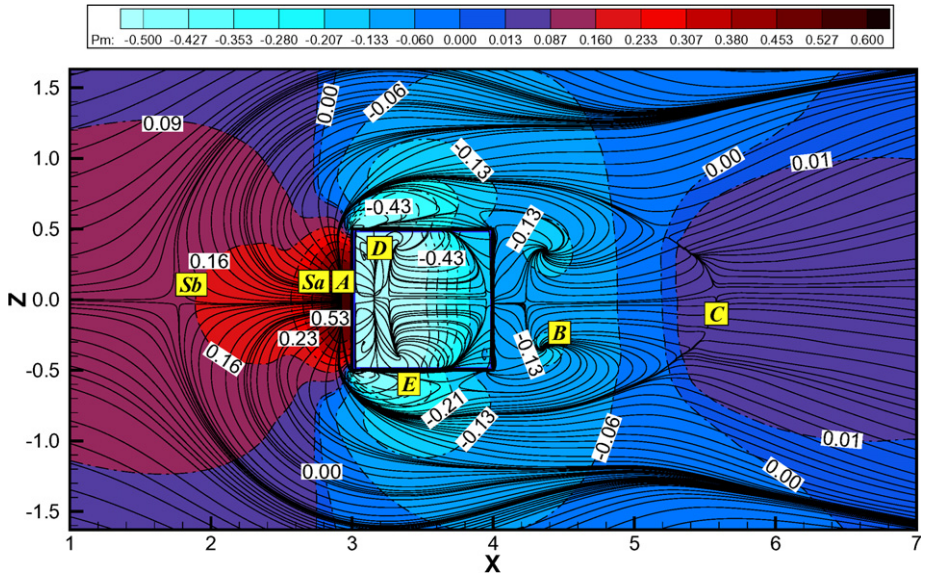

Fig. 4. The near-wall ($y/h = 0.003$) and near-top-surface ($\Delta y/h = 0.003$) distribution of the time-averaged streamlines and pressure.

behind the cube can be easily observed. The areas of rotating flow show the footprints of the arch vortex. In the rear of the cube, the shear layer separated at the top leading edge reattaches at approximately $1.5h$ cube height downstream to the trailing face (marked C). Fig. 4 shows also the near-top cube's surface projected onto the channel floor. This imprint clearly shows two counter-rotating vortices (marked D), which were also observed in the oil-film results of Meinders et al. (1999).

The correlation between the time-averaged pressure distribution and flow structure can be seen in Figs. 2 and 4. A high pressure region is found in front where the oncoming flow impinges upon the cube. The maximum value of the pressure is observed on the cube front face where the front stagnation point appears. In the vicinity of the downstream corners, the top and side vortices separation yields the minimum pressure.

The time-averaged streamlines in the xz-plane for different y/h levels are shown in Fig. 5a–d for one half a channel. The side recirculation region extends upward along the lateral faces. We can see that substantial alteration of its size was not detected. On the other hand, the arc-type vortical structure in the wake, gradually grows towards the channel floor. Fig. 5a shows the imprint of the horseshoe vortex at $y/h = 0.1$, but the imprint of the horseshoe vortex at $y/h = 0.25$ is hardly detected. Meinders et al. (1999) reported that the horseshoe vortex extends up to approximately half of the cube height. To estimate the horseshoe vortex size, in

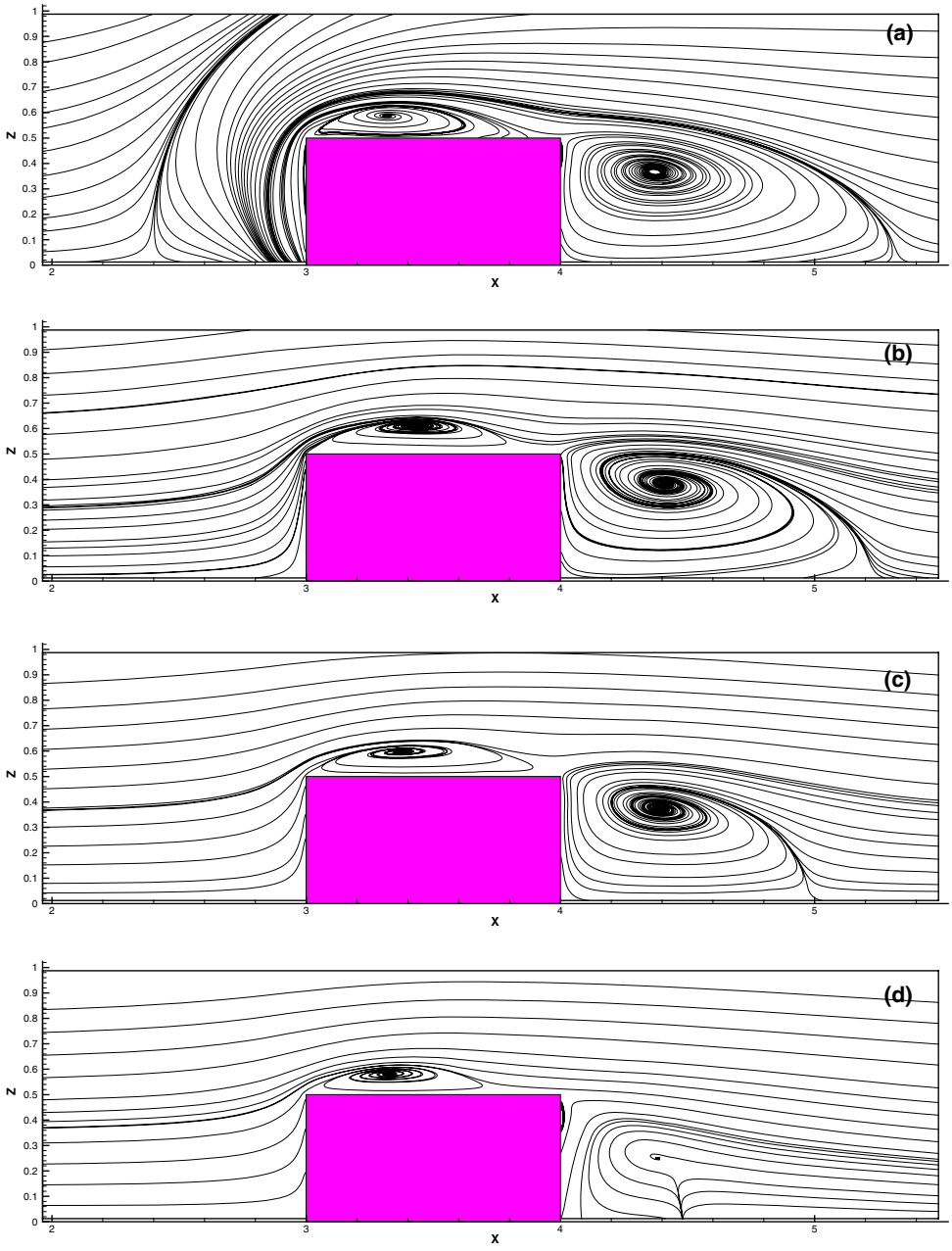

Fig. 5. The time-averaged streamlines in the xz-plane for different y/h levels; $y/h = 0.1$ (a), 0.25 (b), 0.5 (c) and 0.75 (d).

Fig. 6 we show the front view of the time-averaged streamwise vorticity, Ω_x, contour plots for different streamwise x/h-locations in the vicinity of the cube. Only the contours associated with the horseshoe vortex are ad hoc shown in Fig. 6. The converging–diverging nature of the horseshoe-type vortex tube can be observed and its cross-stream size increases with the increase of x/h but does not exceed $0.35h$. The horseshoe vortex is detached from the cube, its distance from the side faces (z_h) and its height (y_h) increase. The increase rate is more intensive from $x_h = 3.11$ to $x_h = 3.50$ than from $x_h = 3.50$ to $x_h = 3.91$. At $x/h = 3.91$, close to the rear face, the vortex tube extends until about $z_h = 0.79h$ and $y_h = 0.34h$.

Fig. 7 depicts the position of the horseshoe vortex in the plane normal to the main flow direction as obtained both in experiments and in our simulations. The Reynolds number in the simulations $Re_h = 5610$ differs from that in the experiments, $Re_h = 40{,}000$. Moreover, we recall that our DNS was carried out in a channel with a ratio of $H/h = 3$ while $H/h = 2$ was used in the experiments of Hussein and Martinuzzi (1996). Nonetheless, the location of the horseshoe vortex is quite similar. To explain this circumstance we refer to Castro et al. (1977) who found that global flow characteristics (e.g. the location of the horseshoe legs, the size of the wake recirculation zone) depend on the boundary layer thickness of the oncoming flow. It appears that the fully developed inlet conditions used in our simulations and experiments led to quite satisfactory agreement in predicting the location of the horseshoe vortex. Krajnović and Davidson (2001) performed LES where the Reynolds number was the same as in the experiments ($Re_h = 40{,}000$), however the inlet velocity profile *was not* fully developed. They, in contrast, found significant difference in the location of the predicted and experimentally observed horseshoe vortex.

Fig. 8 shows the selected time-averaged streamlines. The main vortical structures are clearly seen and are very similar to the "artist's impression" sketch of the flow structure presented in Meinders et al. (1999). Fig. 9 demonstrates that there is good agreement between the time-averaged

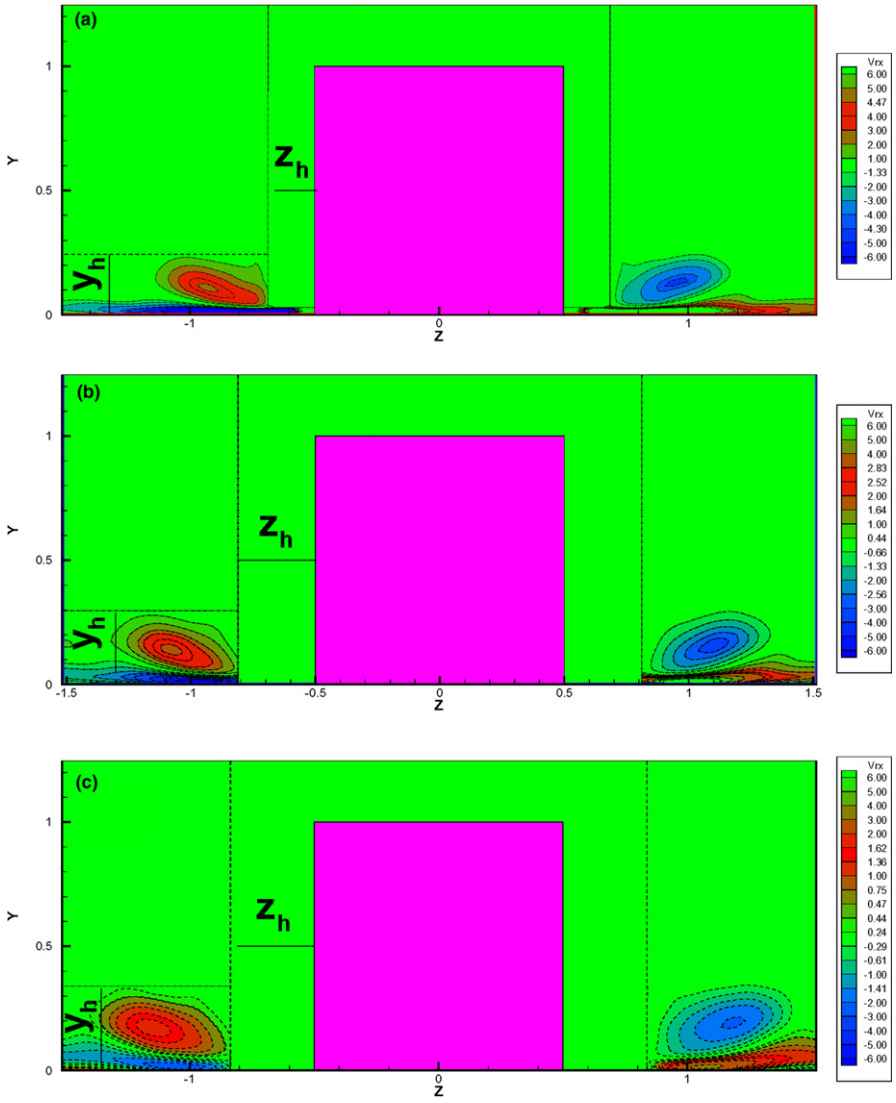

Fig. 6. Time-averaged streamwise vorticity, Ω_x, contour plots for different streamwise x/h-locations: $x/h = 3.11$ (a), 3.50 (b) and 3.91 (c).

streamwise velocity profile normalized by the bulk velocity and the experimental results of Meinders et al. (1999) on the symmetry plane. The consistently larger magnitude of the velocity away from the channel wall may be a result of the smaller channel-height-to-cube-height ratio $H/h = 3$ which were used in our calculations instead of 3.3 as used in Meinders et al. (1999). The quantitative discrepancies in negative mean velocities close to the cube's front and rear faces are related to the aforementioned differences in the horseshoe/arch vortical structures. In their experiments, Martinuzzi and Tropea (1993), Hussein and Martinuzzi (1996) and Meinders et al. (1999) detected dominant fluctuation frequencies sideways behind the cube. It is now well-established that the origin of this unsteadiness is the interaction between the horseshoe vortex and the arch vortex that develops behind the cube. According to the kinematic principles formulated by Hunt et al. (1978), this horseshoe vortex is sidetracked around the edges of the cube into the downstream flow. Fig. 4 shows the imprint of the arch vortex as it detaches from the shear layers shed from the upstream edges of the cube. The legs of the arch vortex lean on a pair of vortices orig-

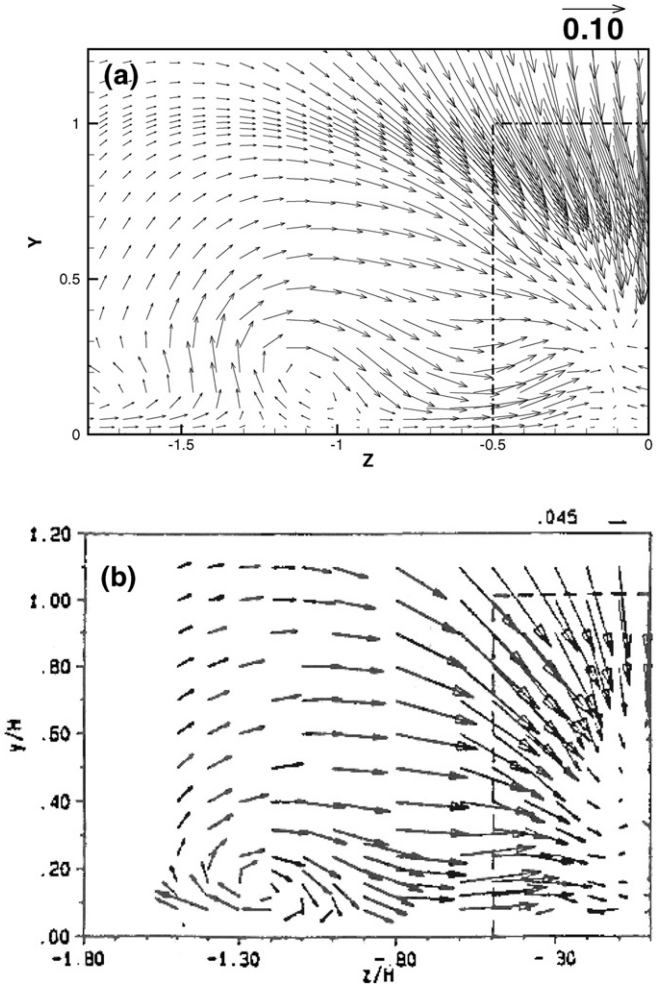

Fig. 7. Time-averaged velocity field in the plane $X/h = 4.75$; (a) present, (b) Hussein and Martinuzzi (1996).

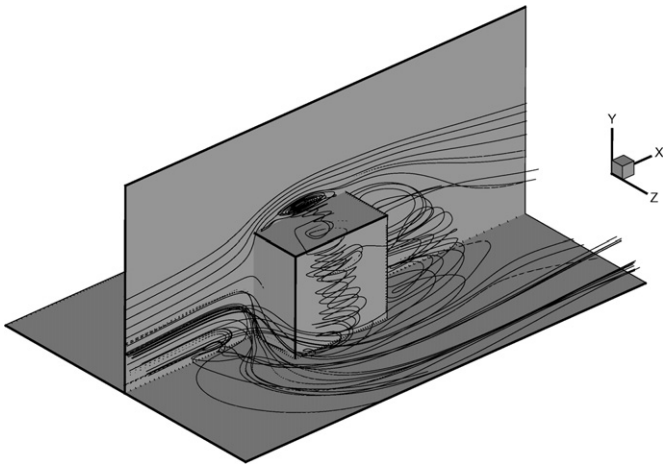

Fig. 8. Time-averaged volume streamlines around a cube.

inating on the channel wall (marked by a focus point "B" in Fig. 4). This focus point illustrates that the vortex entrains part of the fluid carried downstream by the horseshoe vortex. Our DNS-based visualization confirmed the conclusion derived by Hunt et al. (1978), that the entrained part of the side fluid whirls upward, where it is shed into the downstream flow. Unsteady RANS simulations recently performed by Iaccarino et al. (2003) agree with the horseshoe-arch vortices interaction scenario described by Shah and Ferziger (1997). They showed that the vortex pair forming the arch vortex base alternatively intensifies by acquiring vorticity from the flow passing sideways. Owing to this mechanism, the arch vortex legs change their location, which leads to a side-to-side oscillation. To confirm this, a phase-averaging procedure of DNS results should be applied, which has not been carried out during this study.

In our simulations, the dominant characteristic frequency in the rear wake was obtained using FFT analysis of the power spectral density (PSD) of the computed spanwise velocity. The spectrum was obtained from the data collected during about 100 vortex shedding cycles at the point in the symmetry plane $z = 0$ with the coordinates $x/h = 6.0$, $y/h = 0.5$ (see Fig. 3). Fig. 10 shows PSD of the squared spanwise velocity, where a dominant frequency of 0.104 is clearly seen. This value corresponds to the Strouhal number $St = fh/U_m = 0.104$ (based on the cube height h and the bulk velocity U_m) and is consistent with the experimental Strouhal numbers of 0.095 and 0.109 reported in Meinders et al. (1999) and Meinders and Hanjalić (1999), respectively.

4.2. Turbulence statistics

The governing equations were integrated in time until a statistically steady-state was reached. Then the mean flow and turbulence time-averaged statistical quantities were obtained by further time-advancing and averaging. The turbulence mean-square intensities (the normal Reynolds

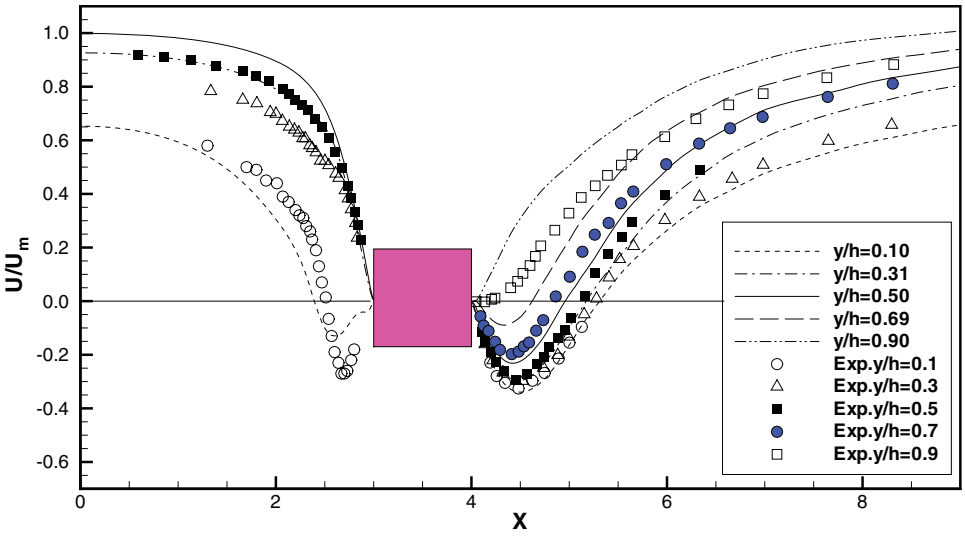

Fig. 9. Time-averaged streamwise velocity in the symmetry plane; symbols: Meinders et al. (1999).

stresses) $\overline{u'^2}$, $\overline{v'^2}$ and $\overline{w'^2}$, kinetic energy $K = 0.5(\overline{u'^2} + \overline{v'^2} + \overline{w'^2})$, energy dissipation rate $\overline{\varepsilon} = \nu\overline{\frac{\partial u_i'}{\partial x_j}\frac{\partial u_i'}{\partial x_j}}$, Reynolds stresses $(\overline{u_i'u_j'})$, and production $(P_K = \overline{u_i'u_j'}S_{ij})$ rate of turbulence kinetic energy were computed using DNS data. The accumulating turbulence statistics and the time-averaged characteristics were performed over about 100 and 30 vortex shedding cycles for the mean-square intensities and second-order moments, respectively.

4.2.1. Turbulence mean-square intensities, kinetic energy, dissipation rate

The contours of the mean-square intensities and kinetic energy dissipation rate in the symmetry plane are shown in Figs. 11a–c and 14, respectively. Our results qualitatively reproduce the results reported in Meinders and Hanjalić (1999). The maxima in the streamwise velocity fluctuations are found in the horseshoe vortex (see the location $X = x/h \approx 2.7$ in Figs. 4 and 11a) and in the top vortices regions where the shear layers separate and reattach. Fig. 11c depicts the spanwise mean-square intensities. The maxima of the spanwise fluctuations in front of the cube occur in the recirculation region and in the vicinity of the front face where the oncoming flow impinges the cube. The difference in the distribution of $\overline{u'^2}$ and $\overline{v'^2}$, $\overline{w'^2}$ mean-square intensities computed above the cube and behind it deserves some comment. First, the distribution of $\overline{v'^2}$ and $\overline{w'^2}$ depicts certain qualitative and quantitative similarities. Second, from Fig. 11a, the turbulence streamwise mean-square intensities $\overline{u'^2}$, generated in the shear layer separated at the leading top edge, reach a maximum in the recirculation region at the top and gradually weaken downstream. Fig. 11b and c reveal the two maxima of the normal and spanwise mean-square intensities $\overline{v'^2}$ and $\overline{w'^2}$, respectively. Aside from the local maximum that occurs in the recirculation region on the top, another occurs approximately at $X = x/h = 5.2$, $Y = y/h = 0.75$. This phenomenon can be attributed to the enhanced mixing in that region (see Fig. 2) and was also found experimentally by Hussein and Martinuzzi (1996).

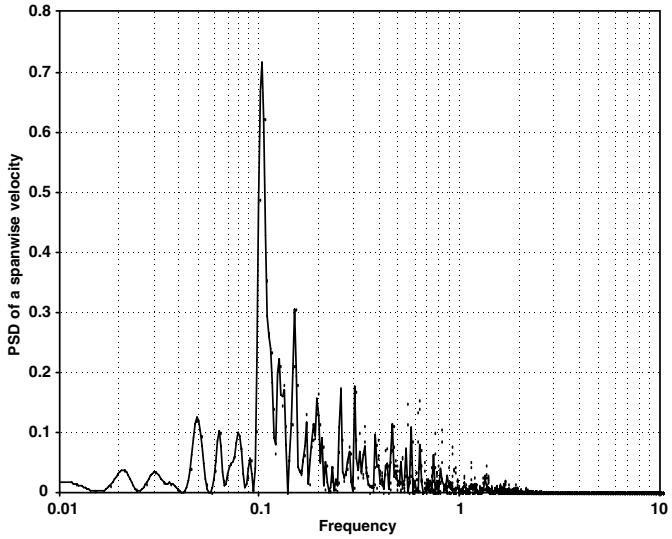

Fig. 10. Power spectrum of the spanwise velocity in the rear wake.

Fig. 12 shows the time-averaged turbulent kinetic energy $K = 0.5(\overline{u'^2} + \overline{v'^2} + \overline{w'^2})$ in the xz-plane for $y/h = 0.1$, 0.25, 0.50 and 0.75 levels. An imprint in Fig. 12(a) indicating the enhancement of turbulence production inside the horseshoe-type vortex is clearly seen. It should be noted that in the side recirculation region, the distribution of the kinetic energy is quasi-two-dimensional (y-independent). From Fig. 12 and from the time-averaged streamlines shown in Fig. 5, one may assume that the side recirculation region is confined into a coherent quasi-two-dimensional vortex. The distribution of the dissipation rate presented in Fig. 13 lends support to this assumption showing very weak dependency in the vertical y-direction in the lateral regions.

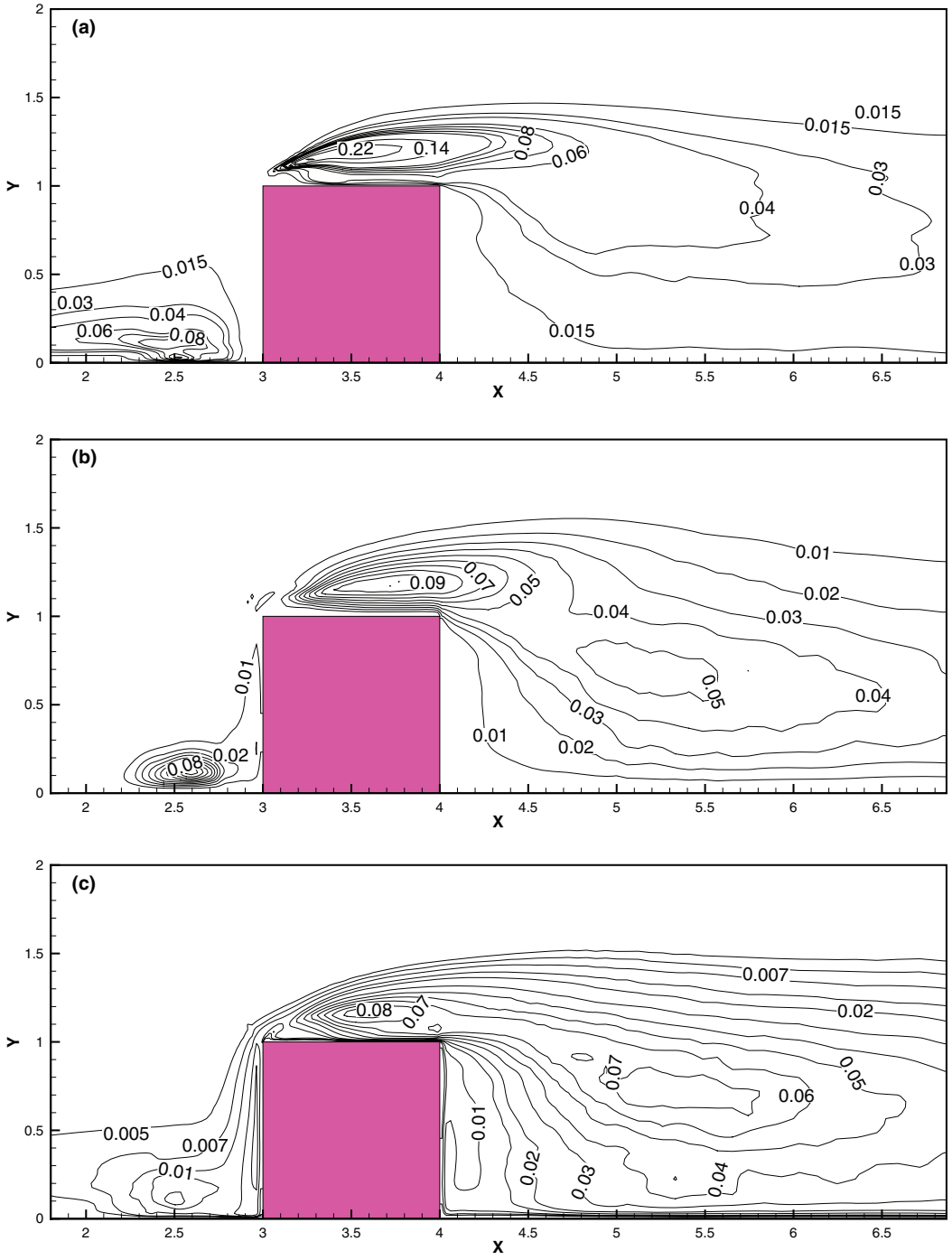

Fig. 11. Mean-square intensities in the symmetry plane $Z = 0$ plane; (a) $\overline{u'^2}$, (b) $\overline{v'^2}$, (c) $\overline{w'^2}$.

4.2.2. Reynolds shear stress

Fig. 15 shows Reynolds stresses $\overline{u'v'}$ in the symmetry plane $Z = 0$. The contours depict the Reynolds stress enhancement in the recirculation region over the cube's top face. The local maxima of $\overline{u'v'}$ clearly observed in front of the cube are discussed below. We performed a numerical experiment in which, for the U and V mean velocity fields obtained from DNS, the Reynolds stresses are calculated from the Bussinesq approximation $-\overline{u'v'} = \nu_t(\frac{\partial U}{\partial y} + \frac{\partial V}{\partial x})$. For $\nu_t = 0.09K^2/\overline{\mathscr{E}}$, the modeled Reynolds stresses are shown in Fig. 16. Figs. 15 and 16 depict a surprising qualitative and quantitative similarity in the recirculation region behind the cube. In front of the cube and on the top, the difference is by a factor of about 2 and 3, respectively, due to overestimated turbulent viscosity.

4.2.3. Negative turbulence production

For complex flows around wall-mounted bluff bodies, one expects that in certain regions (such as those of stagnation) turbulent kinetic energy will exhibit a substantial

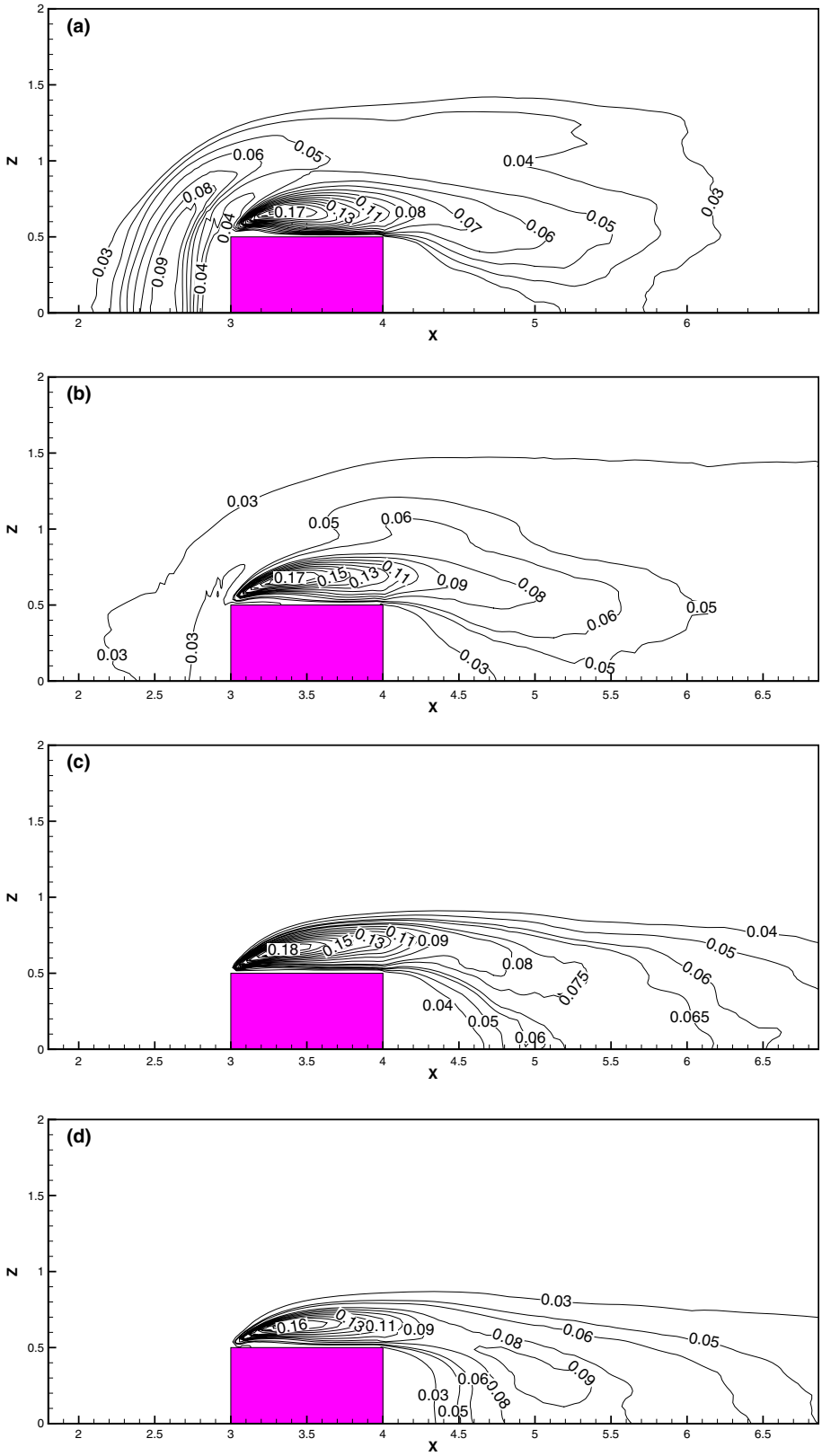

Fig. 12. Contour plots of the turbulent kinetic energy in the xz plane; $y/h = 0.10$ (a), 0.25 (b), 0.50 (c) and 0.75 (d).

decay. Therefore, special concern was given to detect those regions where turbulence production is negative. Negative production points to states that are not in equilibrium and indicates the reverse energy transport from small to large scales. This latter phenomenon is an intrinsic feature of essentially anisotropic flows. For such flows, the energy

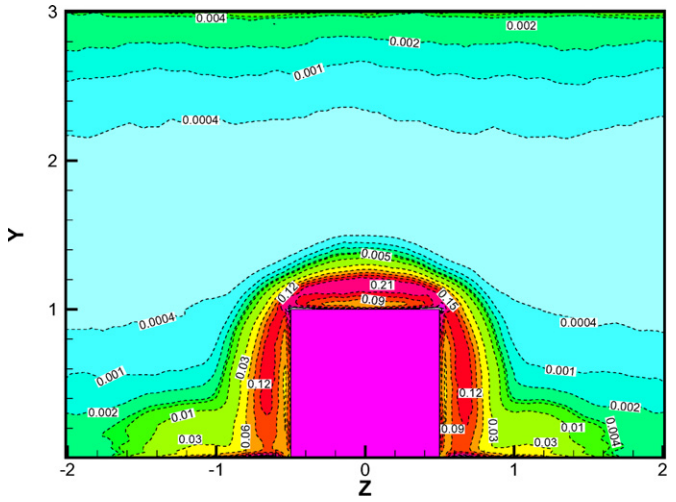

Fig. 13. Contour plots of the dissipation rate $\overline{\varepsilon}$ in the yz-plane, $x/h = 3.5$.

of small scales tends to accumulate into large-scale coherent vortices that dominate the flow. In subgrid scale modeling, reverse transport is known as "backscattering" and is of importance for developing LES approaches (Piomelli et al., 1991). Krajnović and Davidson (1999) predicted that the strongest "backscattering" of energy takes place near the front vertical edges of a cube. In Fig. 17, we show the iso-surfaces and contours of negative production obtained in front of the cube in our calculations. To estimate the individual contributions of the Reynolds stresses to production, we rewrite P_K in the following form:

$$P_K = \frac{1}{2}(P_{uu} + P_{vv} + P_{ww}) \tag{2}$$

$$P_{uu} = -2\left(\overline{u'^2}\frac{\partial U}{\partial x} + \overline{u'v'}\frac{\partial U}{\partial y} + \overline{u'w'}\frac{\partial U}{\partial z}\right) \tag{3}$$

$$P_{vv} = -2\left(\overline{u'v'}\frac{\partial V}{\partial x} + \overline{v'^2}\frac{\partial V}{\partial y} + \overline{v'w'}\frac{\partial V}{\partial z}\right) \tag{4}$$

$$P_{ww} = -2\left(\overline{u'w'}\frac{\partial W}{\partial x} + \overline{v'w'}\frac{\partial W}{\partial y} + \overline{w'^2}\frac{\partial W}{\partial z}\right) \tag{5}$$

The contours of negative values of P_K, P_{uu}, P_{vv} and P_{ww} are shown in Fig. 18a–d. In this region, the oncoming flow impinges on the wall, the flow rapidly decelerates and $\partial U/\partial x$ is negative. The absolute value of $\overline{u'^2}\partial U/\partial x$ is much greater than $\overline{u'v'}\partial U/\partial y$ and $\overline{u'w'}\partial U/\partial z$. As a result, P_{uu} is positive, as can be seen in Fig. 18b where only contours of negative P_{uu} are shown. On the other hand, owing to the incompressibility constraint, negative $\partial U/\partial x$ yields that $\partial V/$

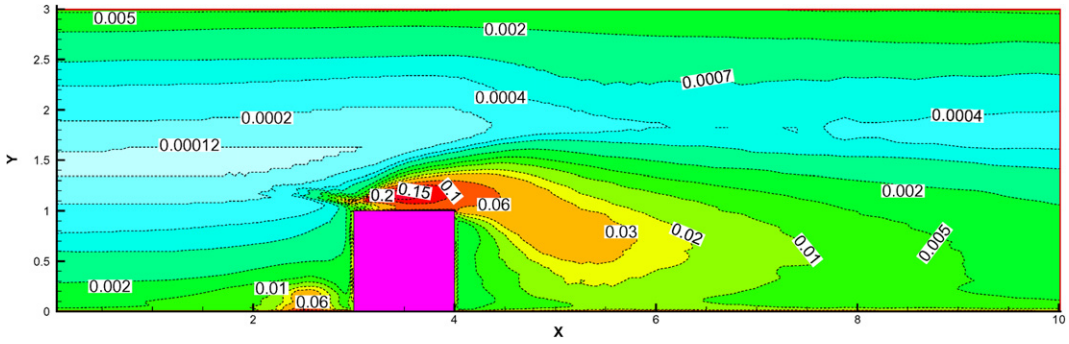

Fig. 14. Contour plots of the dissipation rate $\overline{\varepsilon}$ in the symmetry $Z = 0$ plane.

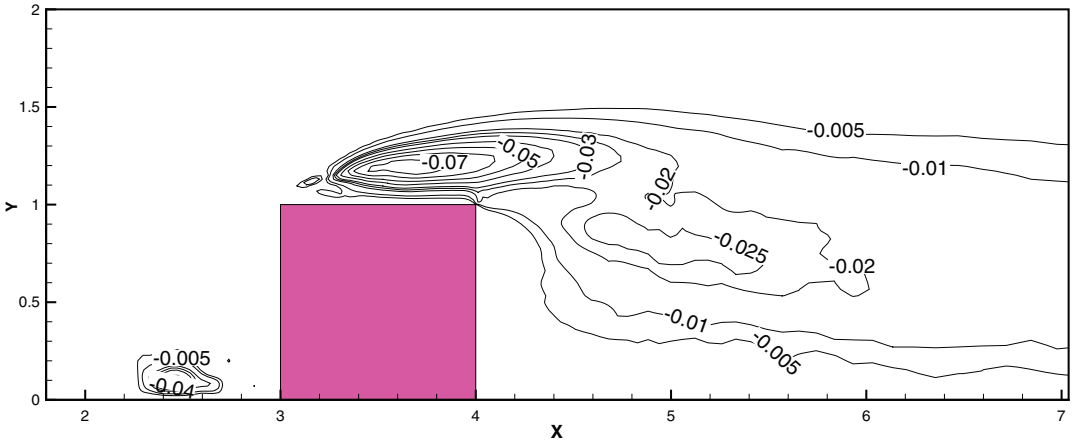

Fig. 15. Reynolds stress $\overline{u'v'}$ in the symmetry plane $Z = 0$.

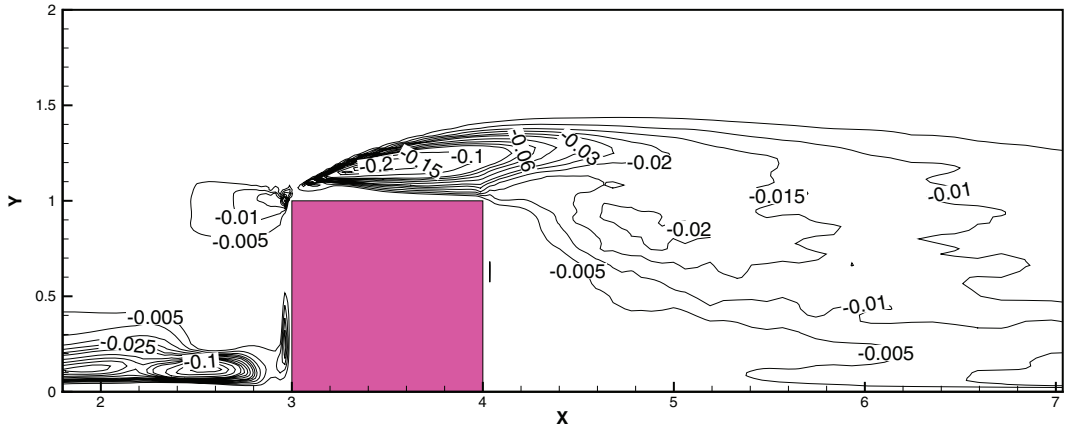

Fig. 16. The modeled Reynolds stresses $\overline{u'v'}$ in the symmetry $Z = 0$ plane; $-\overline{u'v'} = \nu_t(\frac{\partial U}{\partial y} + \frac{\partial V}{\partial x})$, $\nu_t = 0.09K^2/\overline{\varepsilon}$, $K = 0.5(\overline{u'^2} + \overline{v'^2} + \overline{w'^2})$.

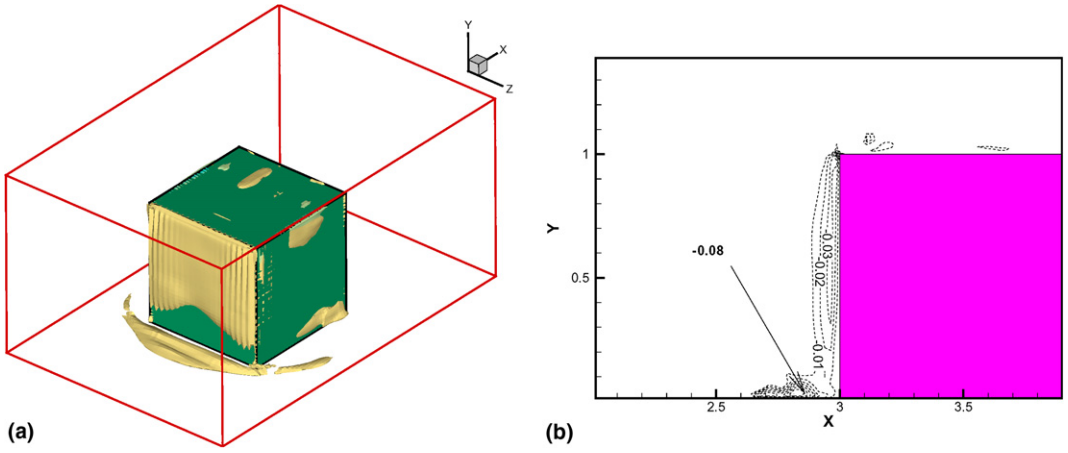

Fig. 17. (a) Iso-surfaces of $P_K = -0.03$ and (b) contours of negative kinetic energy production in the symmetry $Z = 0$ plane.

$\partial y > 0$ and $\partial W/\partial z > 0$. This explains why P_{vv} and P_{ww} become negative near the front wall (see Fig. 18c and d). However, from Fig. 18a, the maximum negative value of $P_K = -0.07$ appears just ahead of the cube, near the channel wall, at $X = x/h = 2.82$, $Y = y/h = 0.035$. This point is in the vicinity of the saddle point marked by "A" in Fig. 4. The situation here is quiet different from that just described. Immediately in front of the cube, below the stagnation streamline marked by "M" in Fig. 2, the flow turns downward and $\partial V/\partial y$ becomes negative near the channel wall. In turn, $\partial U/\partial x$ becomes positive. Furthermore, the terms $\overline{u'v'}\partial U/\partial y$ and $\overline{u'w'}\partial U/\partial z$ are relevant only within the shear layer, which means that $P_{uu} \approx -2\overline{u'^2}\partial U/\partial x < 0$. Fig. 18b shows that mainly the P_{uu} contributes to P_K becoming negative. To explain why P_{ww} is negative, we must turn to Figs. 4, 2 and 8, which depict, with notable agreement, the flow features predicted analytically by Hunt et al. (1978) and observed later experimentally by Martinuzzi and Tropea (1993), Hussein and Martinuzzi (1996) and Meinders et al. (1999). In the region, marked by "A" in Fig. 4, the separation streamline forms a saddle point (Sa in Fig. 4) and the flow is sidetracked forming a horseshoe vortex (Fig. 8). This sideward detachment of a spiral flow implies positive $\partial W/\partial z$, which results in negative P_{ww}. Positive $\partial U/\partial x$ and $\partial W/\partial z$ imply negative $\partial V/\partial y$ and, as a result, positive P_{vv} (not shown in Fig. 18c, where only the contours of negative P_{vv} are shown).

The probability distribution of the u' and w' velocity fluctuations at $x/h = 2.82$, $y/h = 0.04$, $z/h = 0$ show Gaussian distribution. The probability distribution of the vertical fluctuation v' is non-Gaussian with Kurtosis $Ku = 10$ instead of the Gaussian value of 3. The origin of the high Kurtosis can be related to events associated with large-scale instability that appear in this region as the result of negative turbulence production. Based on the above observations, we suggest that flow dynamics in front of the cube is strongly affected by negative energy production.

5. Concluding remarks

Direct numerical simulations were performed on flow around a wall-mounted cube in a fully developed channel flow by using an immersed-boundary method. To minimize any uncertainties related to imposed boundary conditions, we simulated the case of a wall-mounted cube in a fully developed channel flow. Instantaneous results of the

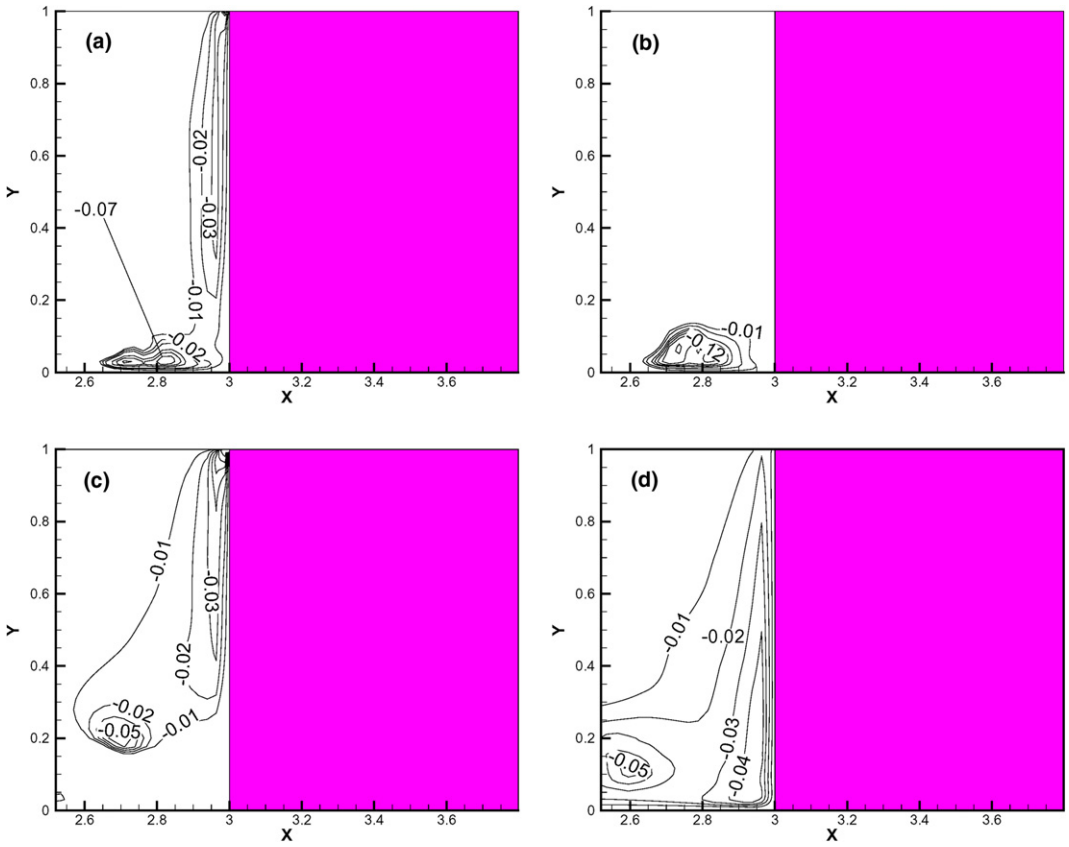

Fig. 18. Contour plots of negative production in front of the cube in the symmetry $z = 0$ plane; (a) P_K, (b) P_{uu}, (c) P_{vv}, (d) P_{ww}.

DNS of a plain channel flow were used as a fully developed inflow condition for the main channel. The Reynolds number, based on the bulk velocity and the channel height, was 5610. The results confirmed the unsteadiness of the considered flow caused by unstable interaction of a horseshoe vortex formed in front of the cube and on both its sides with an arch-type vortex behind the cube. This unsteadiness leads to the vortex shedding phenomenon. The dominant characteristic frequency in the rear wake was detected using FFT analysis of the computed spanwise velocity and agrees with that found experimentally. The time-averaged global flow pattern and characteristics (a horseshoe vortex, an arch-type vortex behind the cube, the length of the recirculation regions) were found to be in good agreement with experimental results.

We presented DNS-based data of the following turbulence statistics: mean-square intensities, Reynolds shear stresses, kinetic energy and dissipation rate. We reported results on negative turbulence production obtained in the region in front of the cube (where the main horseshoe vortex originates). The negative production points to states that are not in equilibrium and indicates the reverse energy transport from small to large scales which is an intrinsic feature of essentially anisotropic flows. The occurrence of negative production in front of the cube can partially explain the failure of some LES/RANS simulations to predict flows around a wall-mounted cube.

Immersed-boundary-based approaches differ by the methods used to introduce an artificial force into the governing equations. The direct forcing method that we used introduces an error of $O(\Delta t^2)$ in the no-slip boundary condition. Implementation of immersed-boundary methods to simulate turbulent flows requires careful monitoring to avoid possible contamination of numerical results arising from inaccurate boundary conditions. One may expect that an error in imposing boundary conditions is unavoidably translated into erroneous predictions. In general, our computations are in good agreement with the experimental findings.

In conclusion, our results lend support to the recent trend to employ immersed-boundary methods formulated on rectangular meshes as a tool for simulating complex turbulent flows.

Acknowledgements

This work was supported by the Israel Science Foundation Grant 159/02 and in part by the CEAR of the Hebrew University of Jerusalem. The third author (NN) was also partially supported by the Russian Foundation for Basic Research under Grant 02-01-00492. The first author (AY) wishes to express his appreciation to Profs. S. Sukoriansky and V. Yakhot for valuable discussions. Our special gratitude goes to the IUCC – the Inter-University Computation

Center, Tel Aviv, where the numerical simulations have been carried out on Cray SV1 supercomputer.

References

Balaras, E., 2004. Modeling complex boundaries using an external force field on fixed cartesian grids in large-eddy simulations. Comput. Fluids 33, 375–404.

Castro, I., Robins, A., Woo, H., 1977. The flow around a surface-mounted cube in uniform and turbulent streams. J. Fluid Mech. 79, 307–335.

Fadlun, E., Verzicco, R., Orlandi, P., Mohd-Yusof, J., 2000. Combined immersed-boundary finite-difference methods for three-dimensional complex flow simulations. J. Comp. Phys. 161, 35–66.

Hunt, J., Abbel, C., Peterka, J., Woo, H., 1978. Kinematic studies of the flows around free or surface-mounted obstacles; applying topology to flow visualization. J. Fluid Mech. 86, 179–200.

Hussein, H., Martinuzzi, R., 1996. Energy balance for turbulent flow around a surface mounted cube placed in a channel. Phys. Fluids 8 (3), 764–780.

Iaccarino, G., Ooi, A., Durbin, P., Behnia, M., 2003. Reynolds averaged simulation of unsteady separated flow. Int. J. Heat Fluid Flow 24, 147–156.

Kim, J., Moin, P., Moser, R., 1987. Turbulence statistics in fully developed channel flow at low Reynolds number. J. Fluid Mech. 177, 133–166.

Kim, J., Kim, D., Choi, H., 2001. An immersed-boundary finite-volume method for simulations of flow in complex geometries. J. Comp. Phys. 171, 132–150.

Krajnović, S., Davidson, L., 1999. Large-eddy simulation of the flow around a surface-mounted cube using a dynamic one-equation subgrid model. In: Banerjee, S., Eaton, J. (Eds.), The First Int. Symp. on Turbulence and Shear Flow Phenomena. Beggel House, Inc., New York.

Krajnović, S., Davidson, L., 2001. Large eddy simulation of the flow around a three-dimensional bluff body. AIAA 2001-0432, 39th AIAA Aerospace Sciences Meeting and Exhibit, Reno, Nevada, 8–11 January.

Lakehal, D., Rodi, W., 1997. Calculation of the flow past a surface-mounted cube with two-layer turbulence models. J. Wind Eng. Ind. Aero. 67&68, 65–78.

Martinuzzi, R., Tropea, C., 1993. The flow around surface-mounted, prismatic obstacles placed in a fully developed channel flow. Trans. ASME, J. Fluid Eng. 115 (1), 85–91.

Meinders, E., Hanjalić, 1999. Vortex structure and heat transfer in turbulent flow over a wall-mounted matrix of cubes. Int. J. Heat Fluid Flow 20, 255–267.

Meinders, E., Hanjalić, 2002. Experimental study of the convective heat transfer from in-line and staggered configurations of two wall-mounted cubes. Int. J. Heat Mass Transfer 45, 465–482.

Meinders, E., van der Meer, T., Hanjalić, K., 1998. Local convective heat transfer from an array of wall-mounted cubes. Int. J. Heat Mass Transfer 41 (2), 335–346.

Meinders, E., Hanjalić, K., Martinuzzi, R., 1999. Experimental study of the local convection heat transfer from a wall-mounted cube in turbulent channel flow. Trans. ASME, J. Heat Transfer 121, 564–573.

Moin, P., Mahesh, K., 1998. Direct numerical simulation: a tool in turbulence research. Ann. Rev. Fluid Mech. 30, 539–578.

Moser, R., Moin, P., 1987. The effects of curvature in wall-bounded turbulent flows. J. Fluid Mech. 175, 479–510.

Nakamura, H., Igarashi, T., Takayuki, T., 2001. Local heat transfer around a wall-mounted cube in the turbulent boundary layer. Int. J. Heat Mass Transfer 44, 3385–3395.

Ničeno, B., Dronkers, A., Hanjalić, K., 2002. Turbulent heat transfer from a multi-layered wall-mounted cube matrix: a large eddy simulation. Int. J. Heat Fluid Flow 23, 173–185.

Nikitin, N., 1996. Statistical characteristics of wall turbulence. Fluid Dyn. 31, 361–370.

Piomelli, U., Cabot, W., Moin, P., Lee, S., 1991. Subgrid-scale backscatter in turbulent and transitional flows. Phys. Fluids A 31, 1766–1771.

Rodi, W., Ferziger, J., Breuer, M., Pourquié, M., 1997. Status of large-eddy simulation: results of a workshop. Trans. ASME, J. Fluid Eng. 119, 248–262.

Shah, K., Ferziger, J., 1997. A fluid mechanicians view of wind engineering: large eddy simulation of flow past a cubic obstacle. J. Wind Eng. Ind. Aero. 67&68, 211–224.

Swarztrauber, P., 1974. A direct method for the discrete solutions of separable elliptic equations. SIAM J. Numer. Anal. 11, 1136–1150.

Tseng, Y., Ferziger, J., 2003. A ghost-cell immersed boundary method for flow in complex geometry. J. Comp. Phys. 192, 593–623.